Effects of excitation laser wavelength on Ly-α and He-α line emission from nitrogen plasmas

S. S. Harilal, G. V. Miloshevsky, T. Sizyuk, and A. Hassanein
Center for Materials Under Extreme Environment, School of Nuclear Engineering, Purdue University, West Lafayette, Indiana 47907, USA

(Received 13 November 2012; accepted 27 December 2012; published online 11 January 2013)

Laser-produced nitrogen plasmas emitting radiation at 2.48 nm (Ly-α) and 2.88 nm (He-α) are considered potential efficient sources for water-window (WW) microscopy. The atomic and optical properties of nitrogen plasma and influence of the laser wavelength on the line emission in the WW range are investigated. It is found that the optimal temperatures for maximum emission from Ly-α and He-α spectral lines are 40-60 eV and 80-100 eV, respectively. The WW line emission and the conversion efficiency (CE) are estimated for three distinct Nd:YAG laser wavelengths (1064 nm, 532 nm, and 266 nm). The calculated CEs are compared with experimentally observed CE values. It is found that 1064 nm wavelength provides the highest CE from laser to Ly-α and He-α radiation.
 [http://dx.doi.org/10.1063/1.4775725]

I. INTRODUCTION

According to Rayleigh criterion, the resolution obtainable with visible microscopy is directly related to the wavelength of the light used, and hence, shorter wavelengths in the soft x-ray region provide higher resolution. Soft x-ray microscopy has the additional advantage of giving access to the WW, which lies between the K-edges of carbon (4.37 nm) and oxygen (2.28 nm). In this region, there is a naturally high contrast between water and carbon rich tissues such as proteins and lipids due to much larger attenuation length for water compared with the organic molecules.[1,2] Furthermore, at these wavelengths, scattering processes (Rayleigh or Compton) are negligible, and hence, there is no contrast degradation due to scattered light as occurs in optical microscopy. Currently, most soft x-ray microscopes use radiation from synchrotron facilities that provide very high spectral brightness due to the small cross section of the electron beam and the narrow radiation cone.[1–5] However, synchrotron use is severely constrained by cost and limited accessibility and requires long term planning and transportation of samples, making this option impractical for most researchers. Potential laboratory-scale WW-transmission x-ray microscopy (TXM) sources are soft x-ray lasers,[6,7] laser-produced plasma (LPP) sources,[8–11] and higher harmonics from laser heated targets.[12,13] WW sources based on LPPs have several advantages over other sources that include power scalability through the tuning of laser parameters, good dose control, flexibility in dimensions, spatial stability, minimum heat load, and a large solid angle of collection.

In the last decade, several groups have worked on developing compact WW-TXM.[14–16] The choice of emission lines in the WW is restricted to the carbon K-α line at 367 eV (3.38 nm), nitrogen Ly-α line at 500 eV (2.48 nm), and nitrogen He-α at 430 eV (2.88 nm).[1] Being on the higher energy side of the WW region, Ly-α and He-α nitrogen lines are more attractive. Another advantage in using nitrogen as target material is that the debris damage from the target to the collection optics is low compared to carbon-bearing targets. In principle, the ideal source should be a target using nitrogen gas puff where the debris from the source is limited to fast atoms/ions. Improvements in LPP sources and imaging optics have led to 50 nm resolutions with a LPP-based WW microscope. Hertz's group[17–20] has developed a LPP-based compact microscope that can operate at two different wavelengths in the WW region and provide a resolution better than 60 nm. Several previous studies have used a liquid nitrogen jet as the source material. Since diffraction optics are used for focusing and imaging, the radiation should be monochromatic. The spectral resolution is determined by the chromatic aberration of the zone plate and typically ranges from $\lambda/\Delta\lambda = 200$ to 1000.

The current status of LPP WW-TXM is such that long exposure times are necessary. This is due to low diffraction efficiency of the focusing zone plates and low conversion efficiency (CE) (conversion from laser to WW line radiation) of the LPP WW light source. This makes data collection for tomography very time consuming. From this, it is clear that enhancing the CE of the soft X-ray source is one of the main elements affecting the viability of LPP-based WW-TXMs. The properties of WW emission from LPP strongly depend on various laser parameters (wavelength, temporal pulse width, spot size, laser intensity, etc.),[21–24] and systematic experimental and modeling studies are necessary to optimize these parameters to provide the highest CE. The situation is similar to optimizing sources for extreme ultraviolet (EUV) lithography at 13.5 nm where significant efforts were made in the last decade, both experimental and modeling, to optimize the source to provide highest CE.[25,26] Laser wavelength is the most important parameter that influences LPP emission intensity in any spectral window, as well as the opacity of the plasma.[21–23] Even though significant efforts are being undertaken to develop WW LPP based sources, to the best of our knowledge, optimization of WW radiation emission has not yet been accomplished with respect to laser wavelength. Moreover, the ongoing modeling efforts directed towards improving the CE in the WW have still not provided significant insight in the mechanisms required to achieve this.

In this article, we investigated the atomic and optical properties of nitrogen plasmas along with the effect of laser wavelength on WW conversion efficiency using the HEIGHTS simulation package.[27–29] We systematically compared the WW emission features from laser plasmas produced by three Nd:YAG wavelengths (1064 nm, 532 nm, and 266 nm). The calculated spectra were visually compared to experimentally recorded spectra from a nitrogen gas jet target as well as emission from boron-nitride (BN) plasma. The estimated CE in WW is compared with reported CE values in the literature. Results show that laser wavelength and laser intensity have a significant effect on the WW conversion efficiency. The paper is organized as follows. In Sec. II, we describe the quantum-mechanical models used for computations of ion composition and photon emission in Ly-α (2.48 nm) and He-α (2.88 nm) spectral lines of nitrogen plasma, and the HEIGHTS package used to study the plasma dynamics and radiative transfer, and the experimental approach. In Sec. III, the results of quantum mechanical calculations, hydrodynamics of nitrogen plasma emitting in the WW region, and the experimental WW spectrum are presented. In Sec. IV, we discuss the CE and compare this with available experimental data. Finally, in Sec. V, the conclusions and recommendations are presented.

II. COMPUTATIONAL MODELS AND EXPERIMENTAL APPROACH

A. Calculation of wavefunctions and atomic characteristics of nitrogen

The self-consistent Hartree-Fock-Slater (HFS) method is used to calculate the wavefunctions, structure of atomic energy levels, transition probabilities, ionization potentials, oscillator strengths, broadening constants, photoionization cross-sections, and other atomic characteristics of nitrogen atoms and ions.[30–32] The non-relativistic HFS method approximately solves the radial Schrödinger equation.[30] Let us consider the *nl*-subshell given by its principal quantum number n and orbital quantum number l with q_{nl} equivalent electrons. For nitrogen, there are 1s, 2s, and 2p subshells with two electrons in each s-subshell and three electrons in the p-subshell. The HFS energy levels correspond to the *nl*-subshells. The non-relativistic Schrödinger equation for a radial wave function $P_{nl}(r)$ in the approximation of *nl*-subshells can be written as follows[30,32]

$$\left(\frac{d^2}{dr^2}+\frac{2Z(r)}{r}+V_{ex}(r)-\frac{l(l+1)}{r^2}+\varepsilon_{nl}\right)P_{nl}(r)=0, \quad (1)$$

where

$$\frac{Z(r)}{r}=\int_r^\infty \frac{1}{r_*^2}\left(Z_0-\int_0^{r_*}\rho(x)dx\right)dr_*,$$
$$V_{ex}(r)=-\frac{3}{2}\left(\frac{3}{\pi}\rho(r)\right)^{1/3},$$
$$\rho(r)=\sum_{nl}q_{nl}P_{nl}^2(r). \quad (2)$$

Here, r is the distance from the nucleus, r_* is the integration variable, ε_{nl} is the binding energy of *nl*-subshell, Z_0 is the nucleus charge, $Z(r)$ is the effective charge of the ion field, $V_{ex}(r)$ is the potential of exchange interaction, and $\rho(r)$ is the electronic density inside the nitrogen atom. The exchange term provides a lowering of the overall energy due to spin correlation keeping like-spin electrons apart. The integral in the expression for $Z(r)/r$ takes into account the inner screening of the nitrogen nucleus by outer electrons. Equation (1) involves the electrostatic and exchange atomic potentials, which are also the subject for determination. They are expressed through the wavefunctions of other atomic electrons. Equation (1) with additional conditions (2) represents the HFS system. The statistical approximation of the $\rho^{1/3}$ type suggested by Slater[33] is used for the exchange potential $V_{ex}(r)$. As the systems (1) and (2) are of an implicit type, they are solved self-consistently using the iterative methods.[32]

The perturbation theory of the non-relativistic HFS wavefunctions is used to account for the relativistic shift effects and spin-orbit interactions thus improving the atomic data. The HFS wavefunctions are used to calculate the Slater integrals that define the direct and exchange electronic interactions between different atomic shells and to determine the matrix elements and transition probabilities for all the types of ions existing in the plasma. For nitrogen, the *LS*-coupling scheme is implemented to represent the energy states and transitions of ions and atoms.[32] In this *LS*-coupling approximation, the electrostatic interaction between electrons has a much greater value than the spin-orbit interaction.

B. Calculation of plasma properties

The quantum mechanical characteristics of nitrogen evaluated with the HFS approach are used in the collisional-radiative equilibrium (CRE) model[32] to calculate the populations of atomic levels, ionization balance, and ion and electron plasma concentrations. The CRE model describes an equilibrium state of the plasma where the rate of collisional processes is exactly balanced by the rate of radiative processes. The collisional processes include collisional excitation and de-excitation, collisional ionization, and three-body recombination. The radiative processes are discrete spontaneous transitions, photo-recombination, and dielectronic recombination. The semi-empirical formulae[32] involving the calculated HFS data are used to evaluate the cross-sections of these collisional and radiative processes. The processes of radiative excitation and photo-ionization are neglected in the CRE model. Therefore, this CRE model satisfactorily describes only the optically thin plasma. For the optically thick plasma, the self-consistent effects due to the non-local radiative flux are taken into account in a simplified form of the escape factor[32] for line transitions and direct photo-ionization for the continuum spectrum. The CRE populations of atomic levels for a range of plasma densities and temperatures are calculated according to the system of kinetic equations[32]

$$\frac{dn_i}{dt}=-n_i\sum_{j\neq i}K_{ij}+\sum_{i\neq j}n_jK_{ji}=0, \quad (3)$$

where n_i and n_j are populations of atomic levels i and j, K_{ij} and K_{ji} are transition rates from level i to other levels j and

from other levels j to this level i, respectively. One equation corresponds to each atomic level. The rates are expressed through the cross-section of collisional and radiative processes using semi-empirical formulae[32] and not detailed here. The system of linear algebraic equation (3) is solved numerically. Equation (3) describes a steady-state case when the atomic transition processes are much faster than thermodynamic changes in the plasma at each hydrodynamic time step. From the calculated population of atomic levels n_i, the ion and electron concentrations, N_i and N_e, are determined for a given plasma density and temperature.[32]

The emission and absorption of photons in plasma originates from three types of radiative transitions: bound-bound, bound-free, and free-free transitions.[32] In the CRE model, the emission coefficient depends on the plasma temperature T, plasma density N, and photon energy ε. It is calculated as the sum of contributions from bound-bound, bound-free, and free-free transitions.[32] Line radiation emitted from bound-bound transitions has a peak of intensity at an energy corresponding to the energy difference between two bound levels. The profiles of spectral lines include natural (radiation damping), Stark, Doppler, and resonance broadening. The main part of the line transitions is non-uniformly distributed over low photon energies with line intensities having non-regular character. The bound-free transitions correspond to ionization/recombination radiation whose energies are the sum of the kinetic energy of the ionizing/recombining electron and the binding energy of the shell that the electron leaves/drops from/to. This radiation is distributed over higher photon energies starting with a discontinuity at the threshold energy corresponding to the binding energy. Bremsstrahlung radiation originates from free-free transitions when a free electron changes its kinetic energy in a collision with electrons and ions. This radiation is distributed over all photon energies.

C. Plasma hydrodynamics and conversion efficiency

The HFS and CRE models are used to calculate the ion and electron composition and optical properties of nitrogen plasma for various densities and temperatures. The data are tabulated and used in the HEIGHTS package[27–29] to model the radiative transport. HEIGHTS package is a set of multipurpose, multiphase, multidimensional computational tools that integrate magnetohydrodynamics (MHD), thermal conduction, atomic and plasma physics, photon transport, and material erosion processes. Currently, HEIGHTS package has numerous integrated models including 3D laser energy deposition and material bulk thermal response, surface melt-layer formation and movement, 3D gas and plasma MHD, and 3-D line and continuum photon radiation transport.[28] HEIGHTS package has been extensively used for estimating the plasma properties as well as the emission efficiency of 13.5 nm plasma sources generated by lasers and discharges.[34,35] Based on the developed physical and mathematical models, HEIGHTS allows complete simulation of LPP evolution and WW photon production. The built-in Monte Carlo models for the laser energy deposition and radiation transport in the entire energy range consider the details of the absorbed, reflected, reabsorbed, and transmitted photons, as well as areas of most intensive absorption and heating. We utilized HEIGHTS in this study for calculating the WW line emission conversion efficiency as well as the density and temperature evolution of laser-produced plasmas from a nitrogen target. The plasma temperature and density given in the article correspond to electron temperature and density, unless stated otherwise.

D. Experimental approach

Both planar BN and nitrogen gas targets were used for generating plasmas. A Q-switched Nd:YAG laser with a pulse duration of ~5 ns at full width half maximum (FWHM) was used to produce plasma with emission in the WW region on approximately the same time scale as the laser pulse. Laser parameters were varied by wavelength and energy. The fundamental wavelength (1064 nm), second harmonic (532 nm), and fourth harmonic (266 nm) of the Nd:YAG laser were used in this experiment to determine the effects of laser wavelength. The laser beam energy at the target surface was attenuated using a combination of waveplate and cube polarizer for all wavelengths. For all three wavelengths, plano-convex spherical lenses of focal length 100 mm were used to focus the laser on the target. The spot diameters at the target surface were estimated using a combination of EUV pinhole imaging of the plasma and OSLO optical design software.[36] The maximum fluences at the target surface were 9.7×10^4 J/cm^2, 1.6×10^5 J/cm^2, and 1.8×10^5 J/cm^2, respectively. The soft x-ray (SXR) spectrum was analyzed using a grazing-incidence spectrograph with a spherical-concave grating that has a groove spacing of 1200 grooves/mm. The spectrograph was positioned at an angle of 45° to the target normal, and the center of the grating was approximately 70 cm from the LPP. The spectrograph slit width was approximately 100 μm. An x-ray sensitive back-illuminated charge-coupled device (CCD) was used to record the time-integrated spectrum. The spectrograph can attain a spectral resolution $(\lambda/\Delta\lambda) \sim 250$ for emission lines in the WW region.

III. RESULTS

A. Ion composition and emission spectra of nitrogen plasma

The ionization energy required to remove the electrons successively from the nitrogen atom and subsequent ions is presented in Table I. The energy to strip off an outermost electron from the neutral nitrogen atom N I is ~14.54 eV. After the removal of this electron, the energy increases since the other electrons are bound more tightly due to the increase in positive charge of the nucleus. The large jump in the energy occurs in going from the ionization of valence electrons (2p subshell (N I, N II, and N III) ions) to the ionization of core electrons (2s and 1s subshells (N IV and N V) and (N VI and N VII) ions). The core electrons are bound more firmly. With the increase in plasma temperature, the degree of ionization and number density of different ions are affected due to these jumps in the ionization energy. Here, plasma temperature is assumed to be electron temperature ≅ ion temperature.

The fraction of free electrons $\alpha = N_e/N$ as a function of nitrogen plasma temperature for different plasma densities is

TABLE I. Successive ionization energies of the nitrogen atom.

N atom/ion	N I	N II	N III	N IV	N V	N VI	N VII
I (eV)	14.54	29.60	47.43	77.45	97.86	552.02	666.83

shown in Fig. 1. The degree of ionization starts to increase from a plasma temperature of ~1 eV onwards. For plasma temperatures, over the range 1–10 eV, the fraction of free electrons α is higher for plasma exhibiting lower densities. With increases in plasma density, the profile slopes up more gradually. For low density plasma $\sim 10^{17}$ cm^{-3}, $\alpha = 5$ is a constant value in a wide range of temperatures from ~10 eV to ~70 eV. This means that the ionization balance of the plasma does not change much in this temperature range. The five electrons from the 2p and 2s subshells are ionized. At higher plasma densities ($\sim 10^{19}$ cm^{-3}), the range of temperatures with the "α-plateau" ionization shrinks. At $N \sim 10^{20}$ cm^{-3}, the "α-plateau" disappears meaning that the fraction of free electrons increases steadily with increasing plasma temperature and average ion charge state within the plasma plume. At a plasma temperature approximately ≥70 eV, the electrons from the 1s subshell are ionized. The fraction of free electrons is larger for denser plasmas ($\sim 10^{19}$ cm^{-3}) compared to that of low-density plasma ($\sim 10^{17}$ cm^{-3}). Finally nitrogen ions are completely ionized at temperature ~300 eV.

The number density of various ions with different charge states in the nitrogen plasma is shown in Fig. 2 for number densities $\sim 10^{18}$ cm^{-3} and $\sim 10^{20}$ cm^{-3}. At low temperatures (<1 eV), the neutral N I atoms predominate. The number density of N I neutrals and singly ionized N II atoms becomes comparable at temperatures of ~1.5 eV (Fig. 2(a)). For denser plasma $\sim 10^{20}$ cm^{-3}, this is achieved at higher temperature ~3 eV (Fig. 2(b)). With further increases temperature up to ~10 eV, the number density of various multi-ionized nitrogen ions changes successively as a function of temperature. For some temperatures (~4 eV, ~6 eV, etc.), the nitrogen plasma is predominantly composed of a distinct set of ions (N III, N IV, etc.) as shown in Fig. 2(a). A plasma state composed of two types of ion species is also possible, e.g., N III and N IV at ~5 eV. These temperature values are shifted toward the greater magnitudes in the case of denser plasma (Fig. 2(b)). The number density of N II and N V ion species shows much broader peaks than those for less denser plasma. The number density of helium-like N VI ions dominates in a wide range of temperatures (~10 to ~60 eV) (Fig. 2(a)). A significant concentration of hydrogen-like N VII ions and stripped N VIII nuclei is achieved at temperatures >60 eV and >100 eV, respectively.

The nitrogen emission spectra are illustrated in Fig. 3 for a plasma density of 10^{19} cm^{-3} and specific plasma temperatures. There is a complicated dependence of the emission coefficient on the wavelength of photons. The presence of sharp "edges" (Fig. 3(a)) in the spectra is due to the bound-free transitions. At temperature ~10 eV, the two high-intensity spectral lines are seen (Fig. 3(a)). On the right-hand side, the strong spectral line of the $1s^2 - 1s2p$ transition at 2.8787 nm corresponds to helium-like N VI ions (He-α). On the left-hand side, the emission line at 2.49 nm is the merger of the two non-resolved lines at 2.4898 nm and 2.4914 nm originating from the $1s^2 - 1s3p$ and $1s^2 - 1s3d$ transitions of helium-like N VI series. The combined emission intensity of

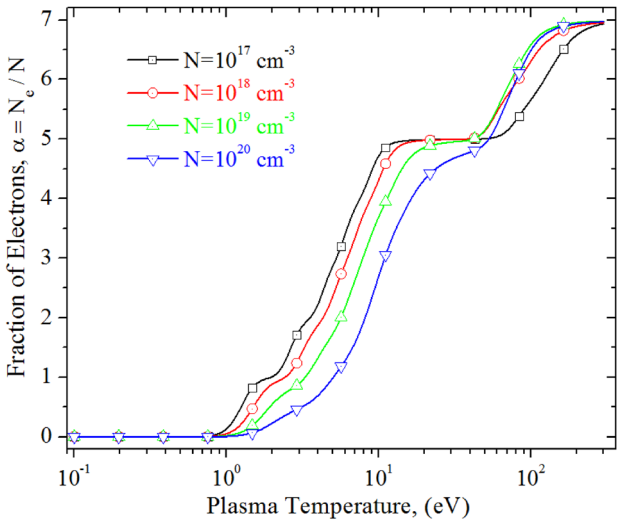

FIG. 1. The fraction of free electrons in a nitrogen plasma as a function of the plasma temperature for different number densities.

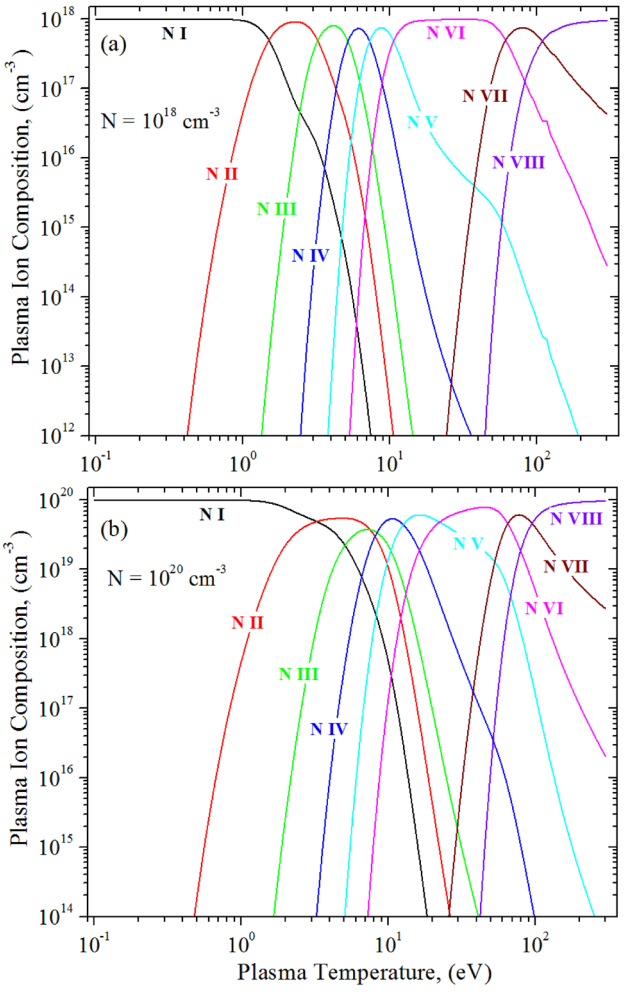

FIG. 2. Plasma ion composition as a function of plasma temperature for different values of plasma density (a) 10^{18} cm^{-3} and (b) 10^{20} cm^{-3}.

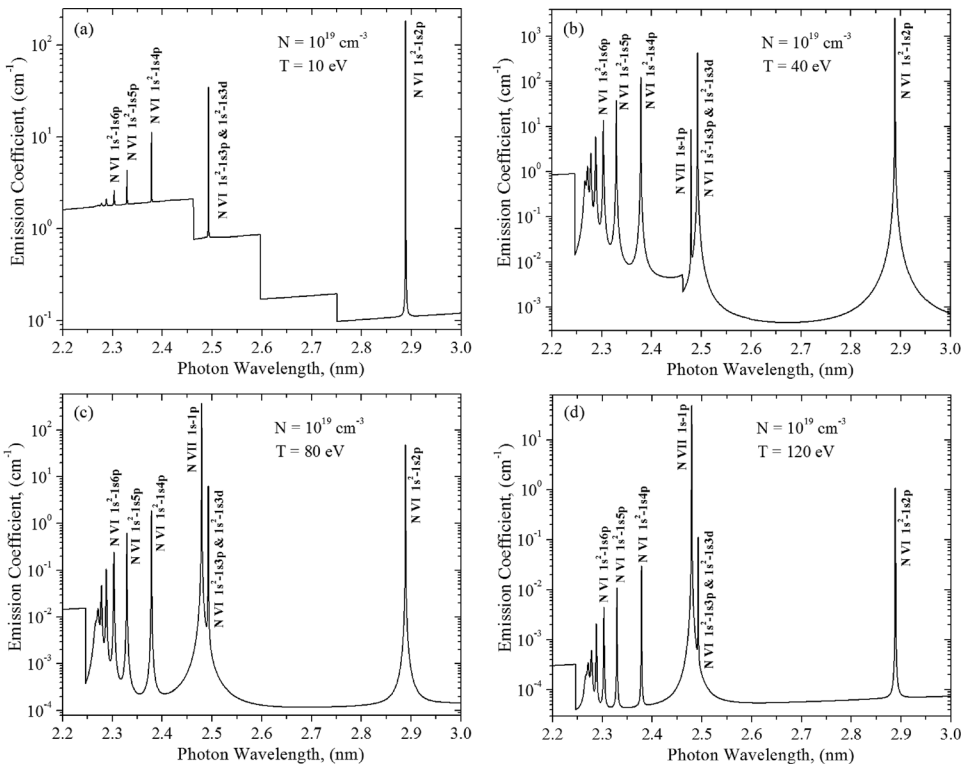

FIG. 3. Calculated synthetic spectra from HFS/CRE models of nitrogen plasma for different plasma temperatures are given for (a) 10 eV, (b) 40 eV, (c) 80 eV, and (d) 120 eV at number density of 10^{19} cm^{-3}.

these two lines at 2.49 nm is about an order of magnitude lower than that of helium-like ions at 2.8787 nm (Fig. 3(a)). At temperatures ~20 eV, the emission of both spectral lines increases by more than an order of magnitude (figure is not shown). The Ly-α line of the $1s - 1p$ transition of hydrogen-like N VII ions at 2.478 nm develops at temperatures of ~40 eV (Fig. 3(b)). The emission of hydrogen-like ions at 2.478 nm is still lower than that of helium-like ions at 2.49 nm. The three spectral lines on the left-hand side of the Ly-α line are due to the $1s^2 - 1s4p$, $1s^2 - 1s5p$, and $1s^2 - 1s6p$ transitions of helium-like N VI ions at 2.3771 nm, 2.3277 nm, and 2.3024 nm, respectively. A group of lines at the leftmost region of the spectrum (<2.4 nm) originate from the higher order transitions of N VI ions. At temperatures of ~60 eV, the 2.478 nm line emission of hydrogen-like ions becomes comparable with the emission of helium-like ions at

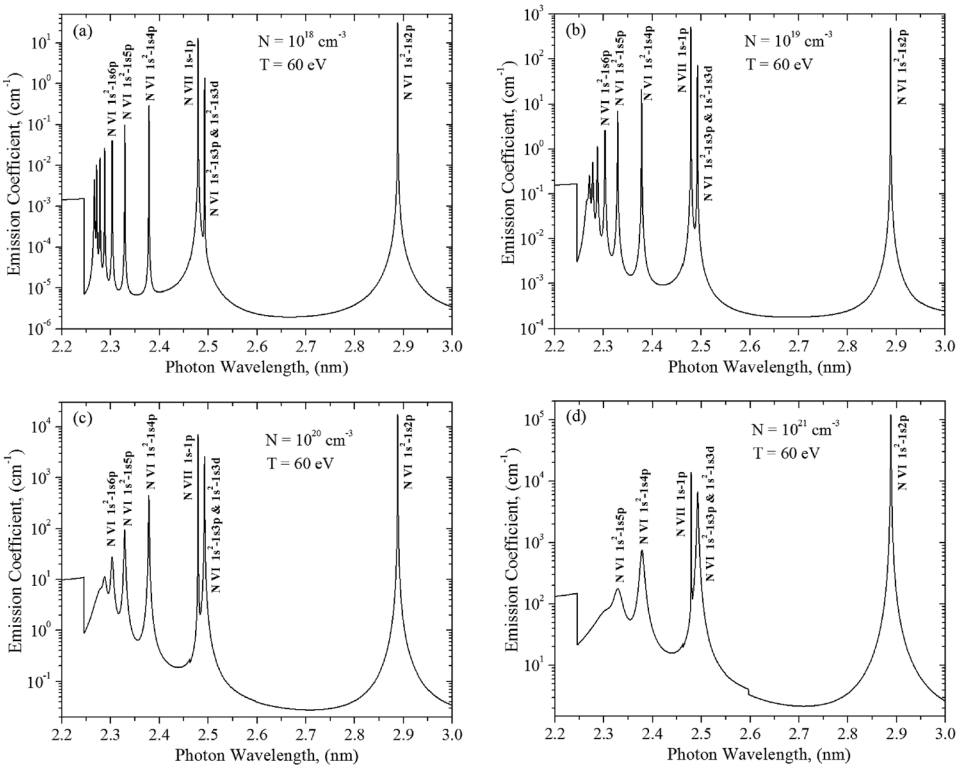

FIG. 4. Calculated synthetic spectra from HFS/CRE models of nitrogen plasma for various plasma number densities (a) 10^{18} cm^{-3}, (b) 10^{19} cm^{-3}, (c) 10^{20} cm^{-3}, and (d) 10^{21} cm^{-3} at a plasma temperature of approximately 60 eV are given.

2.8787 nm, while the emitted intensity at 2.49 nm is reduced by about an order of magnitude (figure is not shown). At this temperature, the concentration of the N VI and N VII ions is nearly equal (Fig. 2). At a temperature ~80 eV, the Ly-α emission overcomes that of helium-like N VI ions at 2.8787 nm (Fig. 3(c)). It becomes dominant by several orders of magnitude at higher temperatures (Fig. 3(d)). However, the Ly-α line intensity decreases because the concentration of N VII ions is gradually reduced at plasma temperatures >100 eV (Fig. 2), while the maximum emission from the Ly-α line can be reached at temperatures of ~80 eV.

The emission spectra of the nitrogen plasma are shown in Fig. 4 for different densities at a temperature ~60 eV. At this temperature, the number density of N VI and N VII ions is comparable (Fig. 2). Therefore, the emission intensity of hydrogen- and helium-like ions in the spectral lines at 2.478 nm and 2.8787 nm is approximately the same (Figs. 4(a) and 4(b)). The emission from these spectral lines increases by an order of magnitude as the plasma density increases by an order of magnitude. At large plasma densities of $\sim 10^{21}$ cm^{-3}, the photon emission from the Ly-α line at 2.478 nm reduces by approximately an order of magnitude compared to that of helium-like N VI ions at 2.8787 nm (Fig. 4(d)).

B. Plasma hydrodynamics and estimation of conversion efficiency

We used the HEIGHTS package for predicting the plasma dynamics and for calculating the CE of both Ly-α and He-α lines at various LPP conditions. The laser wavelengths of interest were 1064, 532, and 266 nm and a pulse, 4 ns (FWHM) in duration was delivered to the target, and the focused spot size was 20 μm. The initial nitrogen density used for the modeling was 0.808 g/cm^3. It should be noted that the size of the target with respect to that of laser spot is an important parameter that governs plasma expansion as well as confinement. Since the size of the target which is significantly larger than the diameter of the focused laser spot, the CE estimation was performed using a planar target and integrating the intensity over 2π sr. The Gaussian temporal distribution better describing an experimental profile of laser pulse is used in our modeling.

The electron temperature and electron density are the parameters that govern the absorption and emission properties of the plasma, and the spatial distribution of these parameters in the nitrogen plasma produced by a Nd:YAG laser with various wavelengths at the peak of the laser intensity is shown in Fig. 5 for time ~4 ns. This time corresponds to the best conditions for efficient output of the Ly-α and He-α radiation. The maximum plasma temperature increases with the increase of laser intensity and decreases at lower intensity. For the considered laser parameters, the WW line displays a similar trend. At a constant intensity of 10^{13} W cm^{-2}, the plasma plume generated by a pulsed, focused laser with a longer wavelength is heated more efficiently. The efficient heating of the plasma is due to the inverse Bremsstrahlung process which has $\sim\lambda^3$ wavelength dependence, and hence, at similar irradiance conditions, hotter plasmas will be produced by laser light with longer wavelengths. For

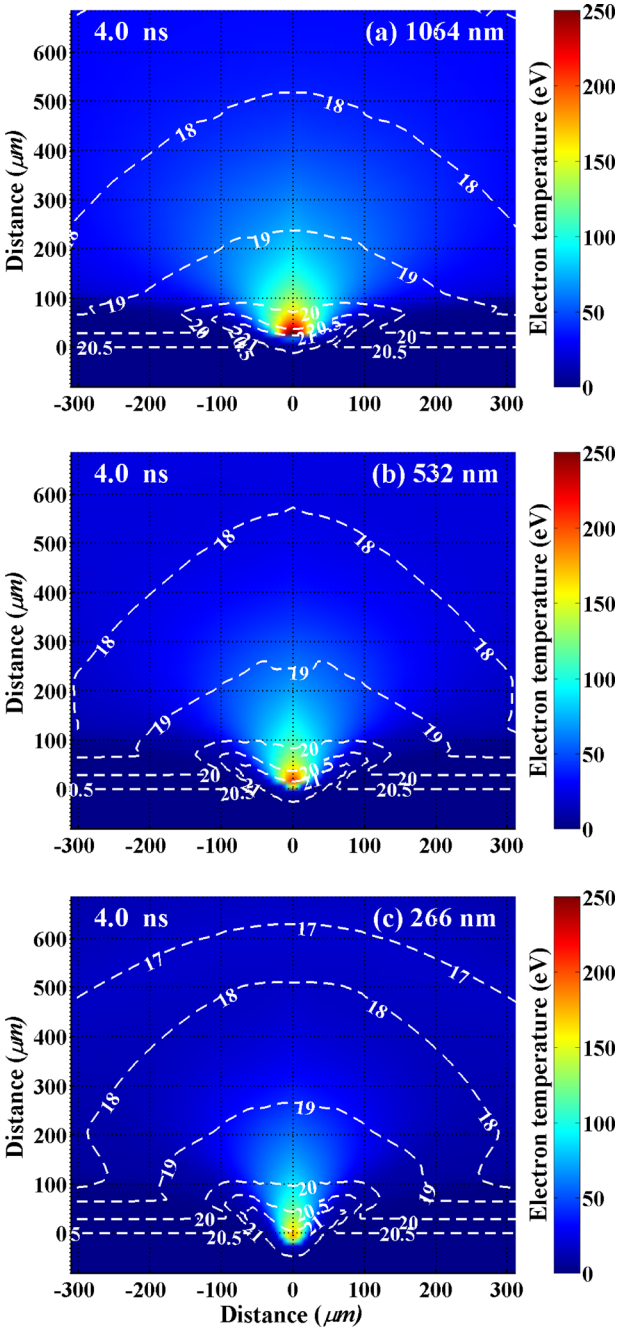

FIG. 5. Simulated hydrodynamic data from HEIGHTS package is given. The spatial distribution of electron temperature and number density at time 4 ns in the nitrogen plasma generated by laser with (a) 1064 nm, (b) 532 nm, and (c) 266 nm wavelengths. The distributions correspond to the intensity peak of laser pulse. The color maps are temperature distributions. The dashed lines indicate equal-density contours, where the numbers are powers of electron density in cm^{-3}.

1064 nm, 532 nm, and 266 nm wavelengths, the estimated maximum temperature is 250, 200, and 160 eV (Fig. 5). The equal density contours (dashed lines) are shown in Fig. 5 in units cm^{-3} with labels indicating the powers of 10. It is seen that the number density of nitrogen plasma ranges from $\sim 10^{17}$ cm^{-3} to $\sim 10^{21}$ cm^{-3}. Although the peak density values show some similarity for plasmas produced by Q-switched pulsed laser with all wavelengths, the density gradient is found to be steeper for plasmas generated by laser pulses with shorter wavelengths. The critical density of the

plasma governs the location of the laser-plasma absorption or reheating processes. For 1064 nm, 532 nm, and 266 nm laser wavelengths, the critical density which scales with wavelength as λ^{-2}, is $1 \times 10^{21}\,cm^{-3}$, $4 \times 10^{21}\,cm^{-3}$, and $1.6 \times 10^{22}\,cm^{-3}$. Hence, laser light with shorter wavelengths can penetrate deeper into core zone of the plasma plume where the electron density (N_e) is higher. This region generally lies closer to the target surface during early time indices. By shortening the wavelength, the laser light interacts more efficiently with a target surface rather than the plasma due to a higher critical density of the plasma for this wavelength. As supporting evidence, the deeper crater was noted for laser ablation with 266 nm pulses (Fig. 5(c)).

Creation of plasma plumes with the best characteristics for maximum emission and minimized absorption of radiation depends on several laser parameters. For the three considered wavelengths, 1064 nm, 532 nm, and 266 nm, the most appropriate conditions occurred at higher laser intensities (Fig. 6). The same laser parameters, such as spot size of 20 -μm and pulse duration of 4 ns, were used for all laser wavelengths. For the estimation of CE of Ly-α, the spectral bin was set up in such a manner that it precludes the emission from the He-β line at 2.49 nm. It is seen in Fig. 6 that the Ly-α and He-α line intensities depend on both laser wavelength and power density. For the whole range of laser power densities, the plasma produced by laser with 1064 nm yields the highest CE for the Ly-α line (Fig. 6(a)). For the He-α line, laser pulse delivery 1064 nm radiation provided the highest CE when the laser power density on the target surface exceeded $10^{13}\,W\,cm^{-2}$ (Fig. 6(b)). At a constant power density $10^{13}\,W\,cm^{-2}$, as shown in Fig. 5, the plasma generated by Nd:YAG fundamental harmonics resulted in the highest temperature. For laser pulses with 266 nm wavelength, the calculated CE was the lowest for both the Ly-α and the He-α lines. This can be explained by the lower temperatures of the developed plasma as well as by the high absorption of WW radiation in cold dense plasma surrounding the region with the most intense emission (Fig. 5).

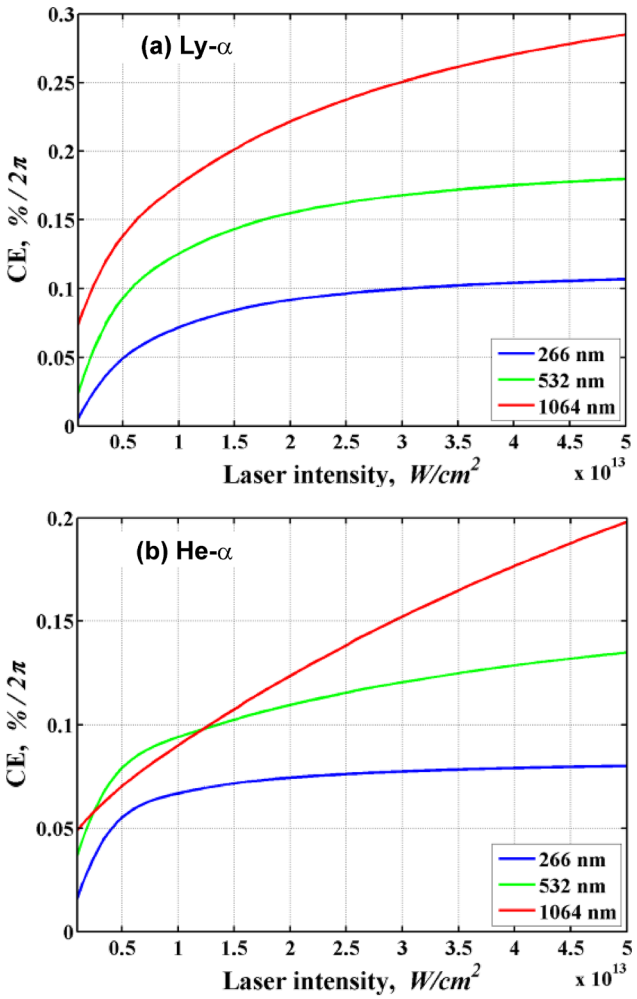

FIG. 6. The calculated CE for (a) Ly-α and (b) He-α spectral lines at laser irradiance conditions with 266 nm, 532 nm, and 1064 nm wavelengths. The estimations were made using HEIGHTS simulation package.

C. Water-window spectral emission

The recorded WW spectra from BN and nitrogen gas jet using 1064 nm laser radiation and at a laser intensity of $10^{13}\,W\,cm^{-2}$ are given in Fig. 7. In both cases (BN or nitrogen jet target), Ly-α and He-α are the strongest lines seen in the spectra. Similar spectral features are seen both with shorter wavelengths (532 nm and 266 nm). Though nitrogen satellite lines are more visible using a nitrogen jet target, their intensity is relatively weak in the BN plasma spectrum. This could be due to large variations in the initial density of the target. The spectra from nitrogen gas jet targets are significantly narrower compared to recorded spectra from BN target. The higher spectral purity is evidently due to the lower density of the gas jet plasma where spectral broadening is minimized. Even though we obtained narrower profiles using gas jet experiments, the He-β line at 2.49 nm is not seen due to the low resolution of the spectrograph used. Since the presence of He-β line is very close to Ly-α, isolation of this line is very difficult and more likely to be seen as a single line.

The peak intensity for Ly-α and He-α lines at various power densities on the BN target for 1064 nm, 532 nm and

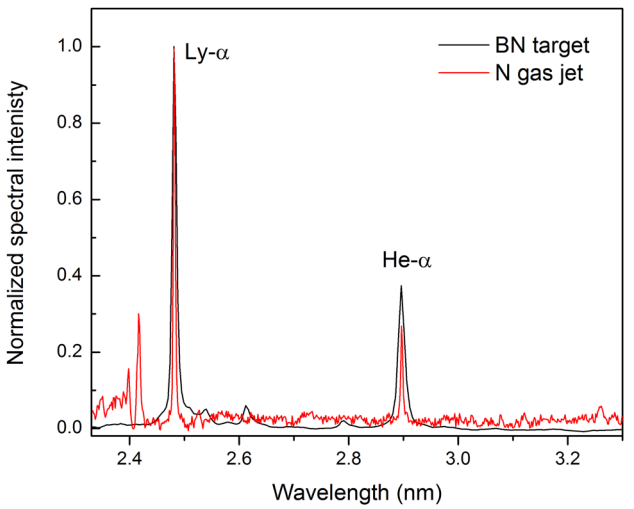

FIG. 7. Experimentally recorded WW spectra from a BN solid target and a nitrogen gas jet target. Nd:YAG laser with wavelength 1064 nm and laser intensity $\sim 10^{13}\,W \cdot cm^{-2}$ was used for generating the nitrogen plasma.

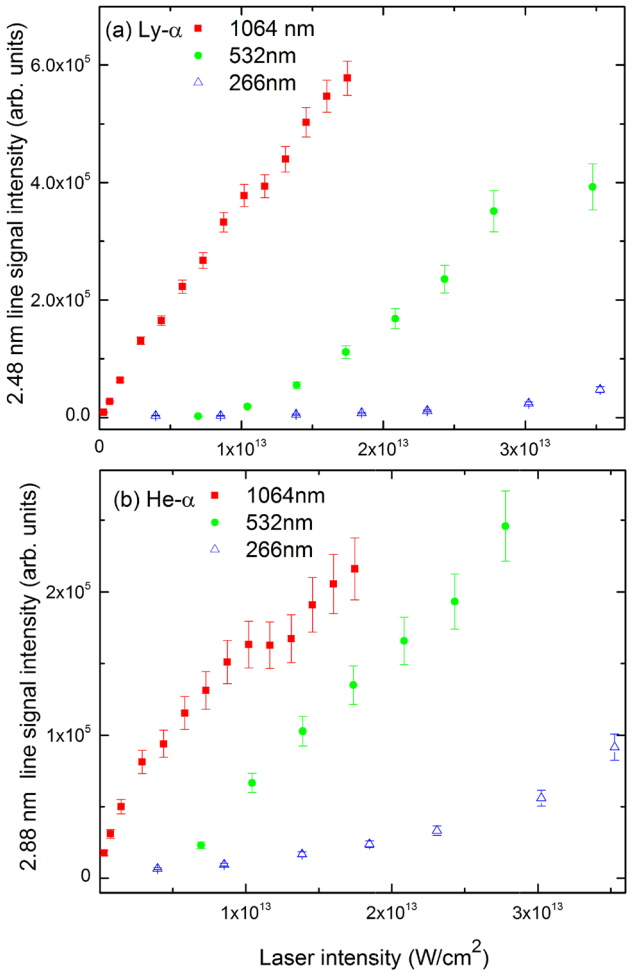

FIG. 8. Intensity changes for (a) N Ly-α and (b) He-α emission lines with respect to laser power density. For plasma plume generation, the radiation from a Nd:YAG laser at fundamental, second and fourth harmonic wavelengths were focused on a BN target.

266 nm are given in Fig. 8. The maximum laser energies available for 1064 nm, 532 nm, and 266 nm were 600, 240, and 90 mJ, respectively. To obtain this data, smaller spot sizes were used for shorter wavelengths to compensate for lower maximum energies at higher harmonics, so equal or higher power densities can be attained. Energy densities in the order of 10^{11}–10^{13} W cm^{-2} were achieved for this experiment. However, it should be remembered that plasma radiation properties can be influenced by laser spot size on the target.[37] Both WW line intensities showed signal enhancement with increasing laser power density irrespective of the wavelength of excitation used. However, for a constant laser power density, the highest and lowest signal levels for Ly-α and He-α lines are obtained for 1064 nm and 266 nm laser excitation.

IV. DISCUSSION

Our modeling results showed that the optimum temperatures for exciting Ly-α and He-α spectral lines in the nitrogen plasma are ~80–100 eV and ~40–60 eV, respectively. The maximum CE obtained for both the Ly-α and the He-α spectral lines are for 1064 nm laser excitation except for a small laser intensity window ($0.3–1.2 \times 10^{13}$ W · cm^{-2}) where 532 nm laser excitation exhibited higher CE for He-α. Visual comparison of the calculated and recorded spectra shows that the nitrogen plasma is heated to temperatures >120 eV. Our spectrograph is not absolute intensity calibrated, and hence, it is not possible to estimate the CE values. So we compared the reported CE values of Ly-α and He-α in the literature to the calculated ones. The long exposure times of present LPP source based WW microscopy is due to the low efficiency of diffraction/reflection optics at these wavelengths and low CE of the LPP source. The situation can be improved by increasing the reflectivity of multilayer condensers, increasing the diffraction efficiency of the zone plate, using high repetition rate lasers and improving the CE of the LPP source. It is notable that most of the groups involved in WW LPP source research employ 532 nm Nd:YAG laser pulses for producing plasma sources.[38–40] However, our modeling calculation showed that the highest CE is possible with fundamental radiation from Nd:YAG lasers compared to the harmonics.

In the last decade, several groups have worked on developing compact LPP based WW light sources and reported widely varying CEs for Ly-α and He-α lines.[38,39,41–45] According to the available literature, the overall CE from laser energy to a single WW line varies from 0.01%–1.5%. As noticed in the development of the 13.5 nm LPP sources for EUV lithography, the CE of LPP sources strongly depends on numerous parameters. Although the laser wavelength and intensity are strongly coupled to the CE, the other parameters that can influence CE include the pulse width,[40] spot size,[37] target geometry,[46] target density,[47] etc. All reported CE measurements are based on the assumption of 4π sr isotropic emission, and it must be mentioned that the LPP EUV or x-ray sources show angular dependency in emission properties and this angular emission property is strongly influenced by target geometry as well as laser excitation wavelength.[22,46,48] For example, Yamaura *et al.*[49] reported that EUV emission exhibits angular dependence with the excitation wavelength with shorter wavelength (4ω) showing a sharper distribution ($\cos^{1.5}\theta$) compared to longer wavelengths, ω, LPP ($\cos^{0.5}\theta$). Moreover, the methodologies used for estimating the CE differ widely between published papers (calibrated spectrographs and using area integration of the spectral lines, spectral peak intensity, photodiodes with metallic filters, etc.). Hence, a direct correlation between the experimental results is rather difficult. Previous studies also showed that ns duration (0.25–10 ns) laser pulses provide higher CE compared to fs short pulses, and this indicates that laser-plasma coupling is important for effective heating and hence temperature stabilization along with increasing the lifetime of the plume.[39,40] Usage of sub-nanosecond pulses leads to the generation of extremely high temperature plasmas. In turn, this results in huge energy loss by hydrodynamic forces driven by large density gradient.

Table II gives the reported CE by different groups for both Ly-α and He-α line intensities. Jansson *et al.*[38] reported ~0.8% and 1% CE for Ly-α and He-α radiation output assuming 4π sr isotropic emission from 3 ns, 532 nm excited liquid

TABLE II. Reported CE by different groups for both Ly-α and He-α line intensities. The experimental details (laser, target, focusing conditions) are also given. All reported CE measurements are based on the assumption of 4π sr isotropic emission.

Laser specifications	Target specifications	CE Ly-α	CE He-α	Selected references
Nd:YAG 532 nm, FWHM 3 ns spot diameter ~15 μm $I = 8.2 \times 10^{12}$–3.7×10^{13} W cm^{-2}	Target: Liquid N jet, diameter ~18 μm	0.8%–0.5%	1.0%–0.4%	Jansson *et al.*[38]
Nd:YAG 1064 nm, FWHM 13 ns spot diameter ~30 μm	Cryogenic planar N target	0.142%	0.25%	Lebert *et al.*[41]
$I = 1.3 \times 10^{13}$ W cm^{-2}	BN target	0.14%	0.2%	
Nd:YAG 532 nm, FWHM 3 ns spot diameter ~10 μm $I = 2.0 \times 10^{13}$ W cm^{-2}	Cryogenic liquid N jet diameter ~30 μm	0.16%	0.1%	Wieland *et al.*[40]
Ti-Sapphire 800 nm, FWHM 250 ps, Spot diameter ~40 μm		0.25%	0.15%	
Ti-Sapphire 800 nm, FWHM 250 ps, Spot diameter ~40 μm		0.013%	0.011%	
Nd:YAG 1064 nm, FWHM 4 ns spot diameter ~30 μm $I = 1.3 \times 10^{13}$ W cm^{-2}	N gas puff target		0.53%	Wachulak *et al.*[43]
Nd:YAG 532 nm, FWHM 120 ps spot diameter ~20 μm $I = 1.5 \times 10^{14}$ W cm^{-2}	Liquid N jet diameter ~10 μm		1.5%	Kim *et al.*[39]
Ti-Sapphire 800 nm, FWHM 500 fs, Spot diameter ~20 μm $I = 2 \times 10^{15}$ W cm^{-2}			0.98%	

nitrogen plasma at a laser intensity $\sim 8 \times 10^{12}$ W · cm^{-2} using a calibrated transmission grating spectrograph which are in reasonably good agreement with estimated values in the present work. However, surprisingly, their measured CE values were found to decrease with increasing laser intensity, which is contradictory to the estimated values in the present paper. For example, they reported a CE of 0.8% at a laser intensity of 8.2×10^{12} W · cm^{-2} which then decreased to 0.46% when the laser intensity was increased to 3.7×10^{13} W cm^{-2}. The decrease in CE with increasing laser intensity could be related to overheating of the plasma or inefficient laser-plasma coupling considering the use of nearly similar liquid nitrogen jet and laser spot diameters (~15 μm). Lebert *et al.*[41] estimated a CE of 0.142%, 0.138% for Ly-α and 0.25%, 0.207% for He-α lines from planar cryogenic nitrogen and BN plasma, respectively, from 13 ns, 1064 nm laser heated plasma at 1.3×10^{13} W/cm^2. Wieland *et al.*[40] measured a CE of 0.16% and 0.097% for Ly-α and He-α lines using calibrated spectrograph system using 3 ns, 532 nm laser excited cryogenic liquid nitrogen target at an intensity of 2×10^{13} W cm^{-2}. They employed calibrated imaging spectrograph containing an off-axis reflection zone-plate for CE estimation and assumed plasma emission into a solid angle of 4π sr. Recently, Wachulak *et al*. developed a 1064 nm heated LPP WW source using a gas puff target and reported 0.53% CE for He-α line. Based on the reported CE values for different wavelengths of excitation, a definite conclusion regarding the optimum wavelength is rather difficult. The discrepancy between the experimentally measured CE and the calculated CE could be due to several factors, and hence, more detailed analysis is required to determine the influence of laser beam parameters as well as target geometry on efficient WW radiation output. Self-consistent modeling will elucidate the discrepancy in CE values from different reported experimental results.

For obtaining the highest possible CE, conditions for high plasma density with stable optimum temperature should be created. The plasma temperature stability is provided by the balance between the incoming and escaping energy, i.e., laser energy absorption, radiation energy loss, and plasma expansion where plasma expansion is mainly controlled by hydrodynamic and geometrical confinement. For imaging thicker samples, it is better to use the higher energy photons source (2.48 nm source instead of 2.88 nm source) because of less attenuation by water along with availability of more photons and hence the requirement of lower dose.[1] However, as shown in the spectral calculation, it is not possible to isolate the Ly-α line from the He-β line considering the typical temperatures and densities of LPP sources. Currently, diffractive optics are the only source of the objective, and hence, the radiation should be nearly monochromatic for obtaining the highest resolution. Considering the spectral purity of the He-α line, it is more attractive for zone pate objective based WW microscopy.

V. CONCLUSIONS

We investigated the atomic and optical properties of nitrogen plasmas along with the laser excitation wavelength dependence on water-window radiation emission. The ion composition and emission spectra of nitrogen plasma in the water-window region were calculated using the HFS and CRE models. The computations were performed for a wide range of plasma temperatures and densities. It was found that the emission of helium-like N VI ions at 2.88 nm can be achieved at a plasma temperature ~10 eV, and then it dominates in over a wide range of temperatures up to ~60 eV. The optimum emission for the He-α line can be achieved at a temperature of ~40–60 eV. It has been established that the emission of hydrogen-like N VII ions at 2.478 nm starts at a temperature ~40 eV and becomes comparable to that of helium-like N VI ions at ~60 eV. At higher temperatures, the Ly-α emission at 2.478 nm prevails reaching the maximum intensity at ~80–100 eV, and then decreases due to the reduction in the number density of N VII ions at temperatures ≥100 eV. Thus, we conclude that the optimal temperature for the maximum Ly-α emission is around ~80–100 eV. With increasing plasma density, the emission of Ly-α and He-α lines significantly increases due to the increase of the number of emitting ions. Therefore, the laser should operate in the mode with the power density optimized for the generation of nitrogen plasma with a temperature and density appropriate for the maximum emission either in the He-α or the Ly-α line.

The WW line radiation and hence the CE were estimated for three prominent Nd:YAG laser wavelengths (1064 nm, 532 nm, and 266 nm) using the HEIGHTS simulation package. The calculated CEs were compared with experimentally reported CE values. Our results showed that longer wavelengths provide the highest laser to WW radiation conversion efficiency. Similar to EUV lithography source at 13.5 nm, where CO_2 lasers emitting at 10.6 μm are currently preferred over Nd:YAG 1.06 μm for obtaining higher CE, longer wavelength excitation is better for obtaining higher CE for WW LPP sources. The use of longer wavelengths with pulse durations in the ns range leads to lower critical density LPP, resulting in efficient laser-plasma heating which leads to improved soft x-ray emission from the plasma. Our CE estimation inferred that the optimum CE values achievable for the parameters studied in this work regarding emission from Ly-α and He-β lines are 0.27%, 0.2% for 1064 nm, 0.17%, 0.13% for 532 nm, and 0.1%, 0.08% for 266 nm, respectively, and all calculations are performed by considering emission in 2π sr.

ACKNOWLEDGMENTS

This work is supported by the National Institute of Health (Grant No. 5R21RR026220) and Defense Threat Reduction Agency (Grant No. HDTRA1-11-1-0046). The authors thank Dr. Syed Hassan and Matthew Crank for experimental help.

[1]J. F. Adam, J. P. Moy, and J. Susini, Rev. Sci. Instrum. **76**, 091301 (2005).
[2]C. Jacobsen, Trends Cell Biol. **9**, 44 (1999).
[3]J. Maser, A. Osanna, Y. Wang, C. Jacobsen, J. Kirz, S. Spector, B. Winn, and D. Tennant, J. Microsc. Oxford **197**, 68 (2000).
[4]D. Eichert, L. Gregoratti, B. Kaulich, A. Marcello, P. Melpignano, L. Quaroni, and M. Kiskinova, Anal. Bioanal. Chem. **389**, 1121 (2007).
[5]W. Meyer-Ilse, D. Hamamoto, A. Nair, S. A. Lelievre, G. Denbeaux, L. Johnson, A. L. Pearson, D. Yager, M. A. Legros, and C. A. Larabell, J. Microsc. Oxford **201**, 395 (2001).
[6]J. J. Rocca, E. C. Hammarsten, E. Jankowska, J. Filevich, M. C. Marconi, S. Moon, and V. N. Shlyaptsev, Phys. Plasmas **10**, 2031 (2003).
[7]K. Lan, Y. Q. Zhang, and W. D. Zheng, Phys. Plasmas **6**, 4343 (1999).
[8]R. de Bruijn, K. N. Koshelev, S. V. Zakharov, V. G. Novikov, and F. Bijkerk, Phys. Plasmas **12**, 042701 (2005).
[9]M. Murakami, S. Fujioka, H. Nishimura, T. Ando, N. Ueda, Y. Shimada, and M. Yamaura, Phys. Plasmas **13**, 033107 (2006).
[10]K. Nishihara, A. Sunahara, A. Sasaki, M. Nunami, H. Tanuma, S. Fujioka, Y. Shimada, K. Fujima, H. Furukawa, T. Kato, F. Koike, R. More, M. Murakami, T. Nishikawa, V. Zhakhovskii, K. Gamata, A. Takata, H. Ueda, H. Nishimura, Y. Izawa, N. Miyanaga, and K. Mima, Phys. Plasmas **15**, 056708 (2008).
[11]P. Yeates and E. T. Kennedy, Phys. Plasmas **17**, 093104 (2010).
[12]P. Gibbon, Phys. Rev. Lett. **76**, 50 (1996).
[13]Y. Liu, Q. Dong, X. Peng, Z. Jin, and J. Zhang, Phys. Plasmas **16**, 043301 (2009).
[14]Y. Wang, C. Jacobsen, J. Maser, and A. Osanna, J. Microsc. Oxford **197**, 80 (2000).
[15]P. A. C. Takman, H. Stollberg, G. A. Johansson, A. Holmberg, M. Lindblom, and H. M. Hertz, J. Microsc. Oxford **226**, 175 (2007).
[16]K. W. Kim, Y. Kwon, K. Y. Nam, J. H. Lim, K. G. Kim, K. S. Chon, B. H. Kim, D. E. Kim, J. Kim, B. N. Ahn, H. J. Shin, S. Rah, K. H. Kim, J. S. Chae, D. G. Gweon, D. W. Kang, S. H. Kang, J. Y. Min, K. S. Choi, S. E. Yoon, E. N. Kim, Y. Namba, and K. H. Yoon, Phys. Med. Biol. **51**, N99 (2006).
[17]M. Bertilson, O. von Hofsten, U. Vogt, A. Holmberg, A. E. Christakou, and H. M. Hertz, Opt. Lett. **36**, 2728 (2011).
[18]J. de Groot, O. Hemberg, A. Holmberg, and H. M. Hertz, J. Appl. Phys. **94**, 3717 (2003).
[19]H. M. Hertz, G. A. Johansson, H. Stollberg, J. de Groot, O. Hemberg, A. Holmberg, S. Rehbein, P. Jansson, F. Eriksson, and J. Birch, J. Phys. IV **104**, 115 (2003).
[20]H. M. Hertz, O. von Hofsten, M. Bertilson, U. Vogt, A. Holmberg, J. Reinspach, D. Martz, M. Selin, A. E. Christakou, J. Jerlstrom-Hultqvist, and S. Svard, J. Struc. Biol. **177**, 267 (2012).
[21]M. Lysaght, D. Kilbane, N. Murphy, A. Cummings, P. Dunne, and G. O'Sullivan, Phys. Rev. A **72**, 014502 (2005).
[22]J. R. Freeman, S. S. Harilal, B. Verhoff, and A. Hassanein, Plasma Sources Sci. Technol. **21**, 055003 (2012).
[23]S. S. Harilal, T. Sizyuk, A. Hassanein, D. Campos, P. Hough, and V. Sizyuk, J. Appl. Phys. **109**, 063306 (2011).
[24]M. Crank, S. S. Harilal, S. M. Hassan, and A. Hassanein, J. Appl. Phys. **111**, 033301 (2012).
[25]T. Tomie, J. Micro/Nanolithogr. MEMS MOEMS **11**, 021109 (2012).
[26]G. O'Sullivan and B. Li, J. Micro/Nanolithogr. MEMS MOEMS **11**, 021108 (2012).
[27]A. Hassanein and I. Konkashbaev, J. Nucl. Mater. **273**, 326 (1999).
[28]V. Sizyuk, A. Hassanein, V. Morozov, and T. Sizyuk, "Heights integrated model as instrument for simulation of hydrodynamic, radiation transport, and heat conduction phenomena of laser-produced plasma in EUV applications," Report No. ANL-MCS-CPH-06/56 (Argonne National Laboratory, 2006).
[29]V. Sizyuk, A. Hassanein, V. Morozov, V. Tolkach, T. Sizyuk, and B. Rice, Numer. Heat Trans. A **49**, 215 (2006).
[30]G. Miloshevsky, V. Tolkach, S. Rozin, and G. Shani, Nucl. Instrum. Methods Phys. Res. B **168**, 467 (2000).
[31]G. Miloshevsky, V. Tolkach, G. Shani, and S. Rozin, Nucl. Instrum. Methods Phys. Res. B **192**, 360 (2002).
[32]V. Tolkach, V. Morozov, and A. Hassanein, "Development of comprehensive models for opacities and radiation transport for IFE systems," Report No. ANL-ET/02-23 (Argonne National Laboratory, 2002).
[33]J. C. Slater, Phys. Rev. **81**, 385 (1951).
[34]A. Hassanein, V. Sizyuk, T. Sizyuk, and S. S. Harilal, J. Micro/Nanolithogr. MEMS MOEMS **8**, 041503 (2009).
[35]A. Hassanein, T. Sizyuk, V. Sizyuk, and S. S. Harilal, J. Micro/Nanolithogr. MEMS MOEMS **10**, 033002 (2011).
[36]OSLO optical design software, Lambda Research Corporation, MA.
[37]S. S. Harilal, R. W. Coons, P. Hough, and A. Hassanein, Appl. Phys. Lett. **95**, 221501 (2009).
[38]P. A. C. Jansson, U. Vogt, and H. M. Hertz, Rev. Sci. Instrum. **76**, 043503 (2005).
[39]B. Kim, B. Ahn, D. Lee, J. Kim, and D. Kim, Appl. Phys. Lett. **88**, 141501 (2006).
[40]M. Wieland, M. Faubel, B. Schmidt, U. Vogt, and T. Wilhein, Proc. SPIE **4504**, 62 (2001).
[41]R. Lebert, G. Schriever, T. Wilhein, and B. Niemann, J. Appl. Phys. **84**, 3419 (1998).
[42]J. Son, M. Cho, D. Kim, B. Ahn, and J. Kim, Appl. Phys. Lett. **90**, 261502 (2007).
[43]P. W. Wachulak, A. Bartnik, H. Fiedorowicz, P. Rudawski, R. Jarocki, J. Kostecki, and M. Szczurek, Nucl. Instrum. Methods Phys. Res. B **268**, 1692 (2010).
[44]M. Wieland, U. Vogt, M. Faubel, T. Wilhein, D. Rudolph, and G. Schmahl, AIP Conf. Proc. **507**, 726 (2000).
[45]H. Fiedorowicz, A. Bartnik, M. Horvath, L. Juha, K. Jungwirth, B. Kralikova, J. Krasa, T. Mocek, M. Pfeifer, L. Pina, J. Skala, J. Ullschmied, and J. Wawer, Proc. SPIE **4502**, 47 (2001).
[46]S. S. Harilal, T. Sizyuk, V. Sizyuk, and A. Hassanein, Appl. Phys. Lett. **96**, 111503 (2010).
[47]S. S. Harilal, B. O'Shay, M. S. Tillack, and Y. Tao, J. Phys. D **39**, 484 (2006).
[48]T. Sizyuk and A. Hassanein, J. Appl. Phys. **112**, 033102 (2012).
[49]M. Yamaura, S. Uchida, A. Sunahara, Y. Shimada, H. Nishimura, S. Fujioka, T. Okuno, K. Hashimoto, K. Nagai, T. Norimatsu, K. Nishihara, N. Miyanga, Y. Izawa, and C. Yamanaka, Appl. Phys. Lett. **86**, 181107 (2005).